ELSEVIER

Contents lists available at ScienceDirect

Construction and Building Materials

journal homepage: www.elsevier.com/locate/conbuildmat





Phase segmentation in X-ray CT images of concrete with implications for mesoscale modeling

Mohmad M. Thakur a, Sean Enright b, Ryan C. Hurley a,b,c,*

- ^a Hopkins Extreme Materials Institute, Johns Hopkins University, Baltimore, MD 21218, USA
- ^b Department of Mechanical Engineering, Johns Hopkins University, Baltimore, MD 21218, USA
- ^c Department of Civil and Systems Engineering, Johns Hopkins University, Baltimore, MD 21218, USA

ARTICLE INFO

Keywords: Concrete Phase segmentation X-ray tomography Machine learning Aggregate shape Aggregate size

ABSTRACT

X-ray computed tomography (XRCT) is a valuable tool for characterizing the microstructure of concrete and for developing 3D mesoscale numerical models directly from experimental data. However, the results of imaging and subsequent modeling are reliable only if individual phases can be identified and segmented accurately. Siliceous aggregates and cement paste are difficult to separate in XRCT images because of their similar X-ray attenuation coefficients. This work examines the quality of aggregate phase segmentation in XRCT images using (1) a standard deviation thresholding approach and (2) a random forest classification. Both approaches were validated with ground truth data for concrete samples with different aggregate volume fractions. Our findings show that either approach may successfully be used to segment aggregate phases if appropriate post-processing is performed. However, our results emphasize the critical need to preserve both aggregate size and shape during post-processing as illustrated through mesoscale modeling.

1. Introduction

Concrete is a multi-phase material with different scales of structural and material heterogeneities [1–3]. The mesoscale heterogeneities are considered important for macroscale properties and behaviors such as stiffness, yielding, and damage [4–7]. X-ray computed tomography (XRCT) has emerged as a powerful tool to capture the microstructure of concrete in 3D, typically at the micron scale [8]. When performed during mechanical loading and combined with digital volume correlation (DVC), XRCT provides rich full-field strain data for validating numerical and theoretical predictions of concrete's mechanical behavior [9–11]. Furthermore, the use of mesoscale numerical models of concrete generated from XRCT images provides a means to predict macroscopic mechanical behavior directly from real microstructures and to examine additional load paths and stress states than are possible in a single destructive mechanical test [11–13].

The segmentation of XRCT images of concrete into individual phases remains central to material characterization, digital volume correlation, and the development of mesoscale models. Fig. 1 shows a horizontal slice of XRCT data obtained on a concrete sample with an aggregate volume fraction equal to 0.5 and the corresponding histogram of the intensity values of the 3D data. It can be observed from Fig. 1(b) that the air voids, high-density phases, and the membrane surrounding the concrete sample can each be segmented manually by simple thresholding

based on intensity values or automatically by using Otsu's method [14]. The segmentation of silica aggregates from the surrounding cement paste, however, remains challenging due to the similar X-ray attenuation coefficients of these two phases. The segmentation problem, therefore, largely reduces to bi-phase segmentation, i.e., the segmentation of silica aggregates from the surrounding matrix (cement paste, air voids, and high-density phase). The present work precisely focuses on addressing this problem by considering two image segmentation approaches:

- One approach based on standard deviation thresholding which relies on the fact that aggregates appear homogeneous in their X-ray attenuation compared to the surrounding matrix phase. The variance in material heterogeneity should be reflected in the standard deviation of the intensity values in XRCT images.
- 2. A machine learning approach based on a random forest classifier [15] which includes quantities such as intensity, edge, and texture at different scales as input features. The edge feature such as image gradient norm was used by Tsitova et al. [10,16] to segment aggregates from the cement matrix. The random forest classifier in the present work uses several features including the edge feature, as discussed in later sections.

^{*} Corresponding author at: Hopkins Extreme Materials Institute, Johns Hopkins University, Baltimore, MD 21218, USA. *E-mail addresses:* mthakur3@jh.edu (M.M. Thakur), rhurley6@jhu.edu (R.C. Hurley).

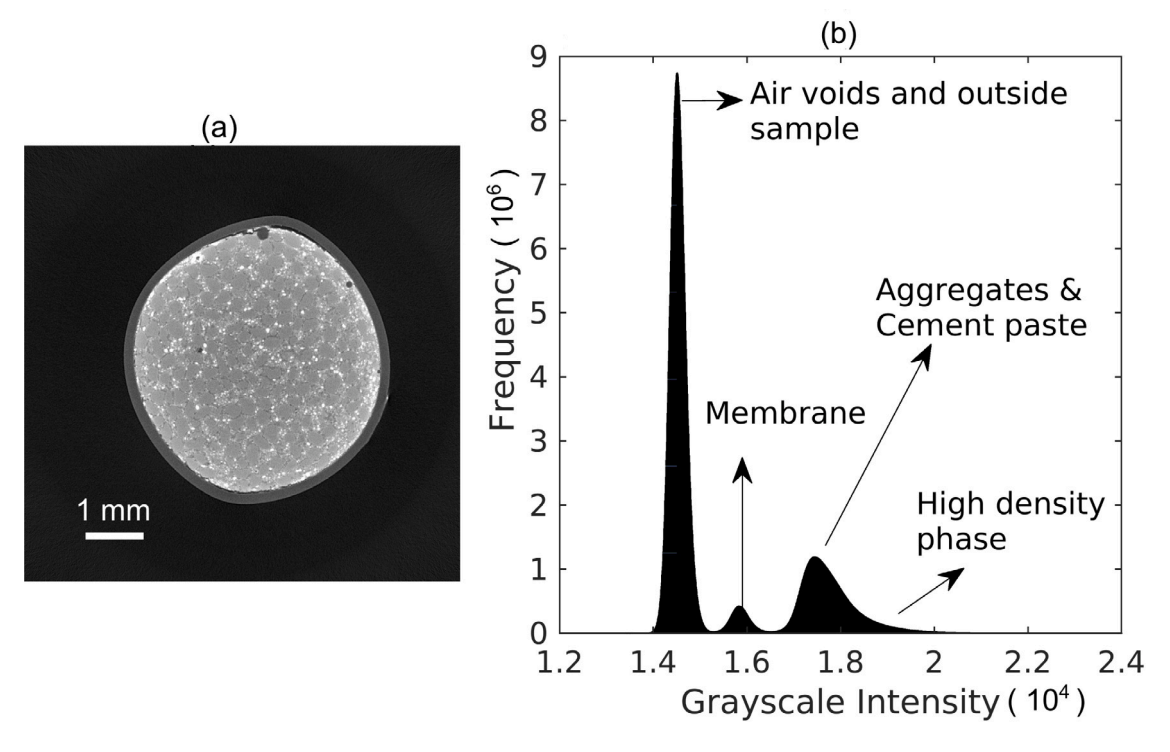


Fig. 1. (a) Horizontal slice of a reconstructed XRCT image with aggregate volume fraction equal to 0.5. (b) Histogram of grayscale intensities of the XRCT slice in (a) showing different peaks for different materials.

The standard deviation thresholding approach of phase segmentation was validated by Stamati et al. [17] for a single concrete sample by comparing the size distribution of aggregates segmented in XRCT images with the corresponding size distribution of the aggregates segmented in neutron tomography images. Hurley and Pagan [7] employed standard deviation thresholding to segment single crystal quartz aggregates from the surrounding cement matrix to study the correlation of fracture nucleation and aggregate stresses. Their work employed in-situ XRCT imaging and 3D X-ray diffraction (3DXRD). They further suggested the possibility of obtaining stresses in the interfacial transition zone once the stress field inside the aggregate is known, which would require precisely segmenting aggregates to capture their size, shape, and surface normals. In another study, Hurley et al. [9] computed volume fractions of different phases in concrete samples from standard deviation thresholding of XRCT images to examine the validity of micromechanics theories in cementitious materials. Thakur et al. [11] emphasized that uncertainties in phase identification could lead to potential errors in the calibration of material parameters in mesoscale models of concrete.

The random forest approach was implemented in open-source software ilastik primarily for phase segmentation in biological images [18–20]. The ilastik software is versatile and easy to use, with no significant programming or computational expertise, unlike deep learning-based image classifiers. ilastik has the potential to become a useful tool and serve the needs of the community in segmenting complex microstructures of cement and concrete composites. To the best of our knowledge, the performance of ilastik has not been systematically examined in segmenting phases in XRCT images of concrete.

At present, several questions related to both phase segmentation approaches, the standard deviation thresholding approach and the random forest approach, remain unanswered and deserve attention:

1. How precisely is aggregate size *and* shape captured in the segmentation of XRCT images of concrete? Both the aggregate size and shape are considered important features in the concrete microstructure [21–23].

- 2. How well do phase segmentation approaches perform when applied to concrete specimens with different aggregate volume fractions?
- 3. What are the implications of phase segmentation in mesoscale modeling of concrete? Can small changes in microstructure due to choices made during phase segmentation lead to large differences in microscale or macroscale response?

In the present work, we examine the segmentation of the aggregate phase and matrix phase for four concrete samples with different aggregate volume fractions using the standard deviation thresholding approach and the random forest approach. The validation strategy includes performing XRCT imaging of dry aggregates prior to concrete sample preparation. The metrics obtained from the XRCT images of dry aggregates serve as ground truth for the validation of phase segmentation results obtained from XRCT images of concrete samples. Our validation metrics include aggregate size distribution as well as aggregate shape descriptors such as sphericity, elongation, and flatness. Finally, we demonstrate through mesoscale simulations the importance of capturing both aggregate size and shape in phase segmentation of XRCT images.

It should be noted that the objective of the present work is to examine the accuracy of phase segmentation approaches in concrete, and not to conduct the most advanced mesoscale simulations possible to understand the mechanics of concrete. In this work, we adopt two-phase mesoscale simulations consisting of aggregate phase and mortar phase. The two-phase mesoscale simulations can capture the aggregate size and aggregate shape comprehensively, and have recently been shown to be capable of capturing stress concentrations at the aggregate-mortar interfaces [11]. While mesoscale simulations can be extended to include a third phase, interfacial transition zones (ITZs), for the most accurate representation of post-failure mechanics, in the present work we avoid modeling ITZ for simplicity because our main focus is on segmentation of the aggregate phase from rest of the cement matrix.

The remainder of the paper is organized as follows. Section 2 describes the materials and methods, including concrete preparation, XRCT image acquisition, both phase segmentation approaches, the

method for validating the approaches, and the mesoscale modeling approach. Section 3 describes the results, including a comparison of the segmentation approaches, emphasizes the importance of morphological operations on the processing of segmented images, and highlights the implications of phase segmentation on mesoscale modeling. The section ends by offering perspectives and guidelines for generating mesoscale models from XRCT images. Section 4 provides a summary of major findings and conclusions.

2. Materials and methods

This section describes XRCT imaging of concrete samples, phase segmentation approaches, data analysis, and the numerical modeling approach performed in this work.

2.1. Sample preparation

The concrete samples were prepared using ordinary portland cement (OPC), ASTM-grade Ottawa sand, and tap water. Ottawa sand is widely used for preparing concrete and is approximately 99.5% SiO₂. ASTM grade Ottawa sand grains were sieved to retain the grains between 200 um and 250 um for concrete preparation. Four samples were prepared with the target aggregate volume fractions equal to 0.2, 0.3, 0.4, and 0.5. Before preparing concrete samples, the aggregates required for each sample were imaged separately in a dry state in an RX Solutions EasyTom 160 MicroCT at Johns Hopkins University. The details related to imaging are provided in more detail in the next subsection. The imaging of dry aggregates was followed by the preparation of concrete samples. Depending on the target aggregate volume fraction, the appropriate amount of dry sand and cement was mixed in a small weighing dish. Tap water was added to the mixture to obtain a water-cement ratio of 0.5 by weight. Additional water was added to the higher aggregate volume fraction samples to achieve similar workability in all the samples. The fresh concrete was then poured into a polymer membrane, and placed on a 3D printed pin to produce a cylindrical sample of diameter equal to 4 mm and of height between 4 and 8 mm. Each specimen was prepared in three layers and each layer was compacted by tamping and vibrating at 200 Hz for 30 s using a table-top vibration machine. The sample was then covered in a small Ziploc bag for 24 h to prevent loss of moisture. After 24 h, a saturated solution of lime was poured into the Ziploc bag containing the specimen. After 28 days, the samples were taken from the saturated lime solution and allowed to air dry at room temperature.

2.2. X-ray computed tomography

XRCT is a non-invasive technique that captures the threedimensional microstructure of the material. XRCT has been extensively used to characterize concrete and other cementitious materials [24-27]. The incident X-rays are attenuated as they pass through the sample. The intensity of the transmitted X-rays can be approximated by the well-known Beer-Lambert Law. The attenuation of the transmitted X-rays is dependent on the energy of the X-rays and the atomic number of the material constituents, which is related to the density. A detailed description of the technique is avoided here for brevity and the interested reader can refer to Refs. [8,28]. In the present study, we used an RX Solutions EasyTom 160 MicroCT at Johns Hopkins University. The main components of the MicroCT system include an X-ray source, a sample stage, and a flat panel detector. The sample is positioned at the center of the rotation stage, between the source and detector, and is rotated about a vertical axis during image acquisition. 2D X-ray radiographs are captured on the flat panel detector as the sample is rotated in small fixed intervals until a full 180° or 360° rotation is completed. The radiographs are then transformed into a 3D volumetric image, in the form of a stack of 2D image slices, based on the reconstruction algorithm (a filtered back-projection in

this study). The voxel size of the resulting images is determined by geometric magnification, or the distance between the cone-beam X-ray source, the sample, and the flat panel detector, and was set to 5 μ m here. The voltage and the current of the X-ray source are important parameters for obtaining good quality data and were set to 80 kV and 120 μ A, respectively, based on our prior experience of working with cementitious materials. A total of 1400 radiographs were captured over a 360° rotation of the sample, and each radiograph was obtained by averaging 6 separate radiographs at a specific angle to reduce the noise.

2.3. Phase segmentation

The segmentation of the aggregate phase from the cement matrix is particularly challenging, as demonstrated in the histogram of intensity values in Fig. 1. It should be noted that this challenge in segmentation arises in the case of siliceous aggregates and not necessarily in the case of other aggregate materials or inclusions. The cement paste and siliceous aggregates exhibit similar X-ray attenuation characteristics. Below we describe phase segmentation approaches – standard deviation thresholding and random forest approaches – and their application to XRCT images of concrete.

2.3.1. Standard deviation thresholding

The standard deviation thresholding approach is based on the premise that the cement matrix exhibits higher grayscale variability in XRCT images (i.e., X-ray attenuation heterogeneity) than the aggregate phase over similar length scales. We demonstrate this in Fig. 2 by plotting grayscale intensity values in a horizontal slice through the XRCT image along a line within the cement matrix and a separate line within the aggregate phase of a concrete sample with an aggregate volume fraction equal to 0.3. It can be observed from Fig. 2(b) that the intensity values in the cement matrix vary significantly compared to intensity values in the aggregate phase. We exploit this feature of intensity variation in segmenting the aggregate phase from the cement matrix in a concrete microstructure. However, instead of examining a line profile, as in Fig. 2, we analyze variability within 3D volumes or structuring elements.

Before performing phase segmentation, the reconstructed XRCT data requires filtering to reduce noise. An anisotropic diffusion filter was applied to the data for this purpose. The standard deviation thresholding approach requires assigning variance or standard deviation to each voxel by computing the standard deviation in its neighborhood. The neighborhood is chosen based on a structuring element. Structuring elements of different shapes can be used such as cubes, spheres, and diamonds [17]. We chose the spherical structuring element due to its geometrical isotropy which prevents biasing the shape of aggregates in any direction. The size of the structuring element used for calculating the standard deviation at each voxel needs to be determined carefully. Ideally, one would choose a size as small as possible but large enough to capture the heterogeneity in the cement matrix. We chose and verified a simple method of determining the size of the structuring element by plotting the histogram of the standard deviation of a 3D XRCT image for different values of the structuring elements. The inbuilt function stdfilt [29] in MATLAB was used to compute the standard deviation map of the data. The 3D array representing XRCT data and the structuring element shape and size are inputs to the stdfilt function. The diameter of the spherical structuring element in MATLAB is equal to $2 \times r + 1$ with values of radius (r) constrained to odd numbers. Fig. 3 shows the plot of the histograms of standard deviation computed at each voxel in an XRCT image of a concrete sample for different diameters of spherical structuring elements. The minimum size of the structuring element that provides two distinct peaks, one representing aggregates and another representing cement matrix, should be chosen as the size of the structuring element for standard deviation filtering. It can be observed from Fig. 3(a) that the spherical structuring element of size 3 voxels does not provide two distinct peaks in the histogram

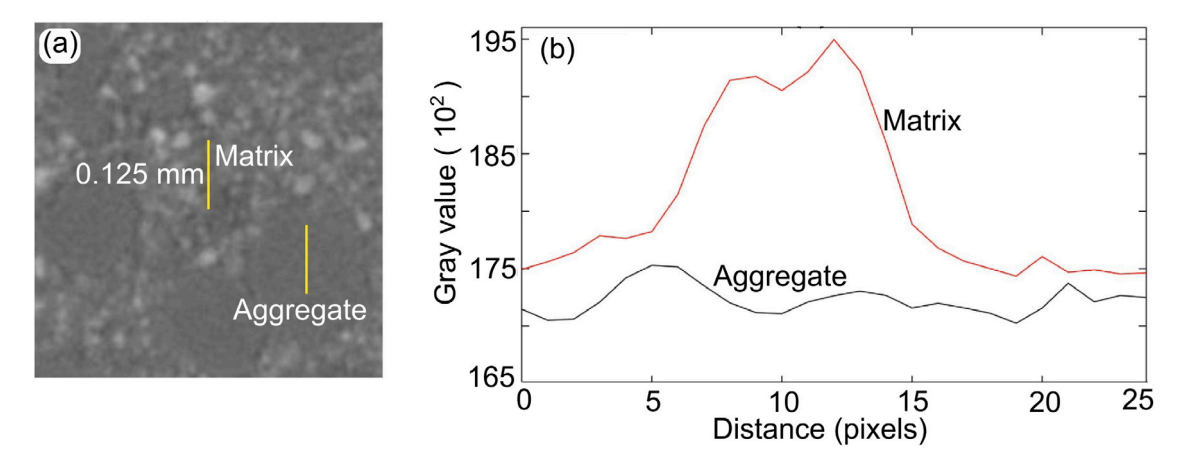


Fig. 2. (a) Region from an XRCT image of a concrete sample with aggregate volume fraction equal to 0.3. Two yellow lines are the regions in the cement matrix and aggregate phase where gray values are measured for demonstration purposes. (b) Grayscale intensity values measured along the yellow lines indicate the heterogeneity in the cement matrix is higher than that in the aggregate. (For interpretation of the references to color in this figure legend, the reader is referred to the web version of this article.)

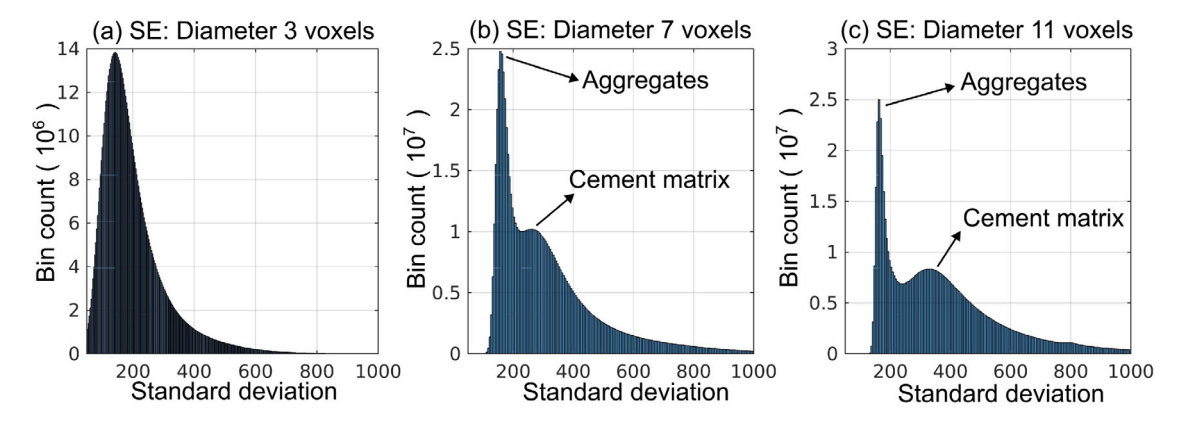


Fig. 3. Determination of the appropriate size of the structuring element (SE). (a) SE of r = 3 voxels produces a single peak in the histogram, therefore not appropriate. (b) SE of r = 7 voxels produces two peaks in the histogram but is larger than the size of SE obtained in (b), therefore preference is given to the size obtained in (b).

plot of standard deviation. Fig. 3(b) and (c) clearly show distinct peaks for spherical structuring elements of diameter equal to 7 voxels and 11 voxels, respectively. Therefore, a spherical structuring element of a diameter equal to 7 voxels is considered appropriate for this particular concrete microstructure.

The workflow for standard deviation thresholding is presented in Fig. 4. The standard deviation of the XRCT data is computed at each voxel based on the appropriate size of the structuring element. Fig. 4(a) and (b) show a slice of the raw data smoothed using an anisotropic diffusion filter and the corresponding slice of the standard deviation map, respectively. The aggregates can be distinguished clearly from the surrounding cement matrix in the standard slice shown in Fig. 4(b). The standard deviation map is binarized by examining the histogram of standard deviation values to separate the aggregates from the cement matrix phase, as shown in Fig. 4(c). In the present work, the threshold for binarization was chosen manually based on the histogram of the standard deviation, such as the one presented in Fig. 3(b). However, one could also choose the threshold for binarization automatically using the Otsu method [14]. The binarization segments aggregates from the cement matrix but underestimates the volume of aggregates and spuriously assigns some small regions in the cement matrix as aggregates. Mathematical morphological operations [9,17,30] are then used to clean the image and retrieve the volume of aggregates as shown in Fig. 4(d). We use open, fill holes, close, and dilation operations in MATLAB to post-process the image and retrieve aggregate volume. The morphological operations should be used carefully to prevent modification of the shape of aggregates, which is discussed further in Section 3.

At this point, the bi-phase segmentation of concrete microstructure into aggregates and cement matrix is complete. If additional phase segmentation is of interest, high-density phases, and air voids can be segmented easily from the smoothed raw data based on an intensity threshold, as shown in Fig. 4(e), which isolates aggregate and cement paste as one phase and air voids and high-density regions as separate phases. Finally, we combine the aggregate phase obtained in Step 4 and air voids and the high-density phases obtained in Step 5 to yield the final segmentation shown in Fig. 4(e). The voxels that do not belong to the aggregate phase, air voids, and high-density phase are assigned to cement paste. It should be noted that voxels belonging to air voids or high-density phases may be assigned as aggregate in the standard deviation threshold but will be assigned correctly in the intensity threshold.

2.3.2. Machine learning approach

The machine-learning approach for image segmentation adopted in this study is a random forest classification, a supervised learning technique. Supervised machine learning requires training data to make predictions. Readers can find more detail on random forest classifiers in Ref. [31]. Random forest classification makes predictions based on an ensemble of decision trees and provides generalized performance compared to other non-linear classifiers because predictions are based on several decision trees. The decision tree includes several binary tests and the overall structure of these tests resembles the structure of a tree. Each tree consists of internal nodes with a test for the input attribute, for instance, in the case of phase segmentation, a test at a node can

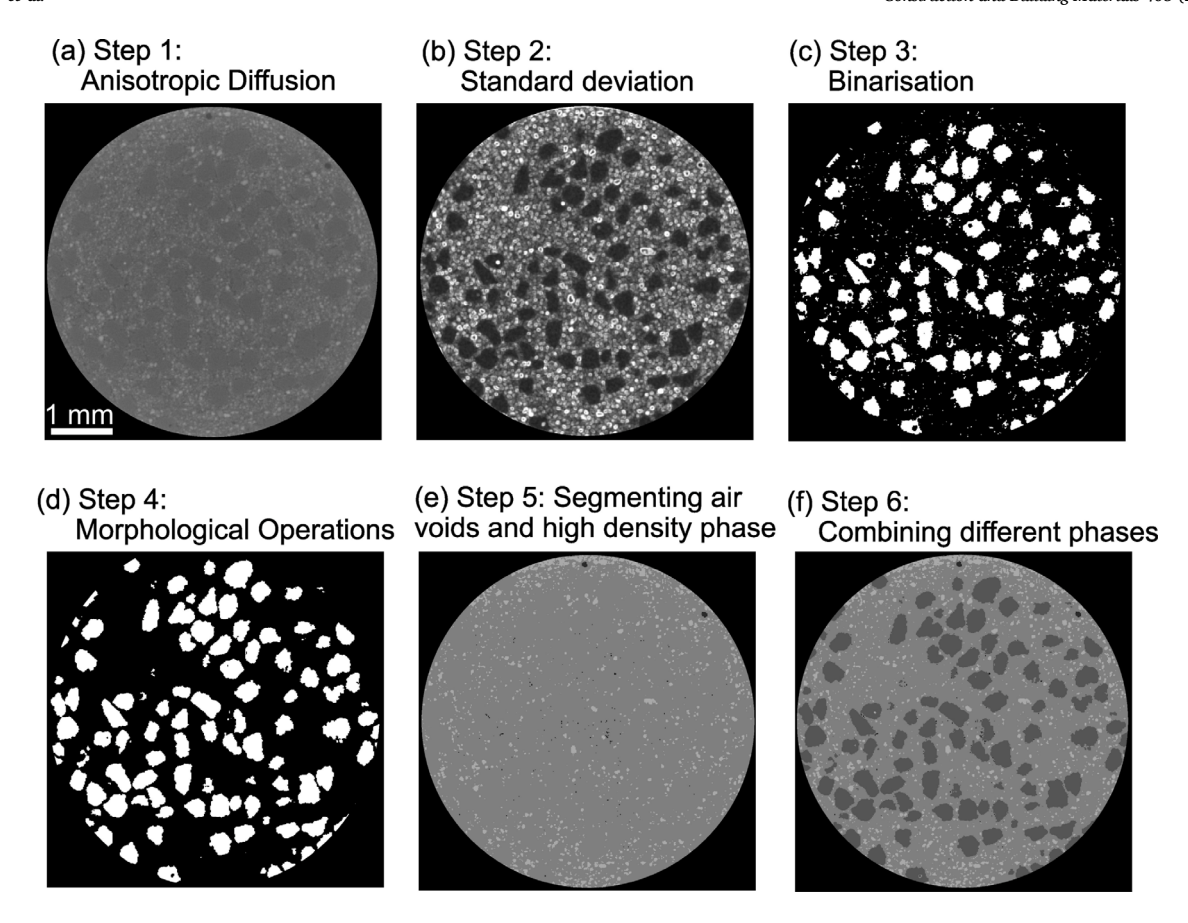


Fig. 4. Workflow for standard deviation thresholding segmentation. An aggregate volume fraction equal to 0.3 is considered here for demonstration. (a) Step 1: Anisotropic diffusion filter applied to raw data to reduce noise. (b) Step 2: Standard deviation of the smoothed data. (c) Step 3: Binarization of standard deviation data. (d) Step 4: Morphological operations to clean data and retrieve the volume of aggregates. (e) Step 5: Segmenting air voids and high-density phase based on the intensity from smoothed data obtained in Step 1. (f) Combine different phases to produce final segmented data.

be whether the intensity of the voxel is below 10 000. Similarly, there can be additional tests in a tree depending on the features we select, as discussed in the next paragraph. The branch of a tree ends with a terminal node which provides the classification label. The final label is assigned by counting the number of votes/decisions from all the decision trees.

The default number of trees in ilastik is equal to 100 and the same number of trees were used in the present work. The developers of ilastik suggest that increasing the number of trees beyond 100 does not improve performance and decreasing the number of trees below 100 results in loss of generalization of the classifier. In the present work, we use the random forest implemented in the pixel classification module of open-source software ilastik [32] to segment aggregates in XRCT images of concrete. The features such as smoothed intensity, edge filters, and texture descriptors at different scales are passed on to the random forest classifier to make a decision in the feature space that is finally projected back with a class/phase assignment to the voxels. An example of the select features that quantify intensity, edge, and texture in the images are shown in Fig. 5. Note the six features in Fig. 5 are provided for a Gaussian smoothing equal to 1.6 sigma (standard deviation). For actual training data, we use Gaussian smoothing equal to 0.7 sigma, 1 sigma, 1.6 sigma, and 3.5 sigma resulting in 25 features in total including an intensity feature with sigma equal to 0.3. Note that the choice of the values of sigma are provided automatically in ilastik, but the user can add particular sigma values as well.

ilastik offers a convenient interface for users with an introductory or moderate background in machine learning. The training process is straightforward: a subset of the data is used for training and labels for phases are annotated by the user using simple brush strokes. The training process is interactive in the sense that brush strokes can be added or removed and the user can observe the influence of training on segmenting phases in training data. However, the user needs to carefully annotate the training data. Furthermore, random forest classification is not a deep learning classifier and more training data does not necessarily improve its performance.

The workflow that we found suitable in ilastik for segmenting aggregates in XRCT images of concrete is described next and presented in Fig. 6. This workflow is similar to the workflow recommended by developers of ilastik for the pixel classification module [33] but features additional considerations specific to XRCT data of concrete. In the present study, training and the corresponding predictions are made separately for each concrete sample. We did not use the same training data for all concrete samples because we observed some changes in the imaging conditions for different samples. The training data is selected from the bottom, middle, and top of the sample to account for any variations in the X-ray intensity due to the conical shape of the beam. The predictions were not as accurate towards the ends of the sample if only the middle region was used for training. Ten consecutive slices were chosen from each region for the training data. More data can be used for training but this would require additional computational resources. In our case, ten slices provided reasonably accurate segmentation, as will be observed in the results section. ilastik has an advantage in that training can be done on less data in predefined feature space compared to the deep learning approaches which train directly on images. A total of 25 features, quantifying intensity, edges, and texture in the XRCT data at different smoothing scales were selected. We chose all features available in ilastik, however, one could reduce the number of features if computational cost is a constraint. Once the features are selected, the training of the data follows by annotating directly on the images, as shown in Fig. 6(c), with live feedback on the segmentation of phases

(a) Intensity: Gaussian smoothing (b) Edge: Laplacian of Gaussian Gradient Magnitude Imm (d) Edge:Difference of Gaussians (e) Texture: Structure tensor Eigen values (f) Texture: Hessian of Gaussian Eigen values

Fig. 5. Visualization of the select features that serve as input to random forest classification in ilastik. An aggregate volume fraction equal to 0.3 is considered here for demonstration. Features here are only shown for the smoothing level of 1.6 sigma (standard deviation), but smoothing levels 0.7 sigma, 1 sigma, 1.6 sigma, and 3.5 sigma are considered. Therefore, a total of 25 features are considered including raw data intensity. (a) Gaussian smoothing of raw data. (b) Laplacian of Gaussian. (c) Gaussian gradient magnitude. (d) Difference of Gaussian. (e) Structure tensor eigenvalues. (f) Hessian of Gaussian eigenvalues.

during training. It is important to annotate from different regions of a slice for the best prediction accuracy. We annotate aggregates near the four diametrically opposite ends, in addition to the center of the samples, as shown in Fig. 6(d). The initial strokes are more important and can influence segmentation significantly compared to the later strokes. The cause for this is rooted in the limitation of random forests, where too much data does not necessarily improve performance in contrast to the case for deep learning approaches. However, the simplicity of the approach compensates for the inability to include large datasets to improve predictions. Once the training process is complete, predictions can be made that assign phases to aggregates and cement matrix, as shown in Fig. 6(e). The predictions were made on the 3D XRCT data of each sample, including the slices that were used for training. The user needs to be careful to use the testing data acquired with similar imaging conditions compared to the training data. Large variations in intensity and the presence of imaging artifacts in testing data that are not present in training data may result in inaccurate phase segmentation.

Similar to standard deviation thresholding, random forest classification also requires the use of morphological operations to clean images, retrieve the volume of aggregates, and assign phases including air voids and high-density phases from intensity thresholding, if desired.

2.4. Validation approach

Our approach to validating the segmentation approaches involved performing XRCT imaging of dry aggregates before preparing each concrete sample. The aggregates in the dry state were poured into a cylindrical polymer membrane that was placed on a 3D-printed pin. XRCT imaging provides high-quality images of aggregates in a dry state due to the high X-ray attenuation contrast between aggregates and air. The segmentation of dry aggregates and air voids is straightforward and can employ intensity thresholds selected manually or using Otsu's

method [14]. The segmented aggregates were then separated into individual grains using the watershed segmentation algorithm in MAT-LAB [34]. The metrics that quantify the size and shape of aggregates were then obtained using the regionprops3 command in Matlab. The volume of the grain was obtained as the number of the voxels belonging to a grain/region separated by watershed segmentation. The equivalent diameter (D_{eq}) of each grain was then obtained as the diameter of a sphere (D_s) equal in volume to the volume of the grain. The grain shape was quantified using three metrics: sphericity (S), elongation index (EI), and flatness index (FI) [35]. Each of the size and shape metrics are defined by

$$D_{eq} = D_s, (1)$$

$$S = \frac{SA_s}{SA},\tag{2}$$

$$EI = \frac{b}{a},\tag{3}$$

$$FI = \frac{c}{b},\tag{4}$$

and were obtained using the region props3 command in MATLAB. SA represents the surface area of the grain, SA_s represents the surface of the equivalent sphere (equal volume) and $a,\ b$ and c represent the maximum, intermediate, and minimum length of the eigenvalues, respectively. The metrics $D_{eq},\ S,\ EI,\$ and FI obtained from XRCT images of dry aggregates served as ground truth for validating phase segmentation approaches. These metrics were compared with the same measures obtained for aggregates in segmented XRCT images of concrete to validate each segmentation approach. The aggregate size, and aggregate shape quantified by metrics such as sphericity and elongation ratio, are important to capture damage initiation in concrete, as demonstrated in the mesoscale simulations in prior work by Naderi et al. [21]

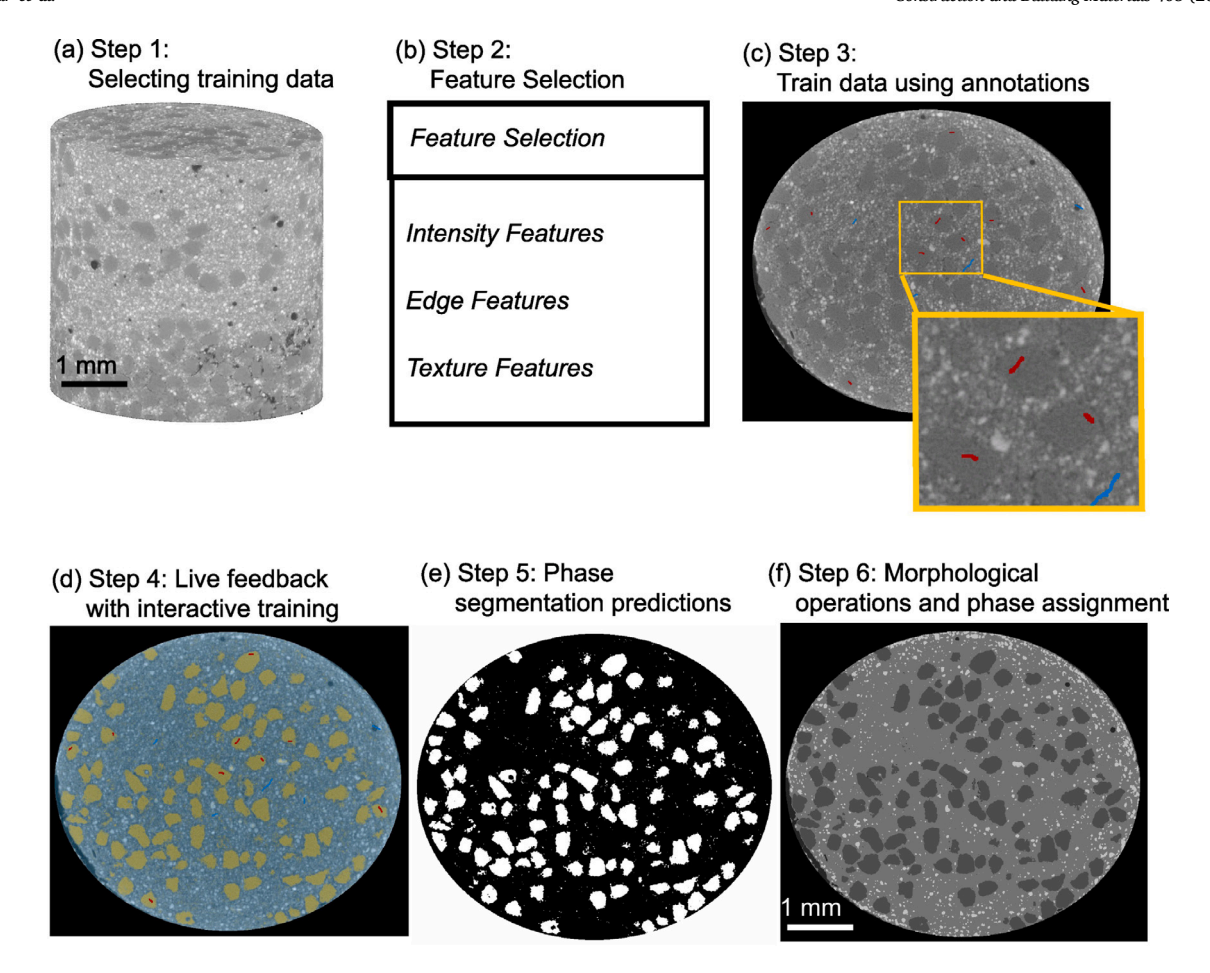


Fig. 6. Workflow for phase segmentation in ilastik. An aggregate volume fraction equal to 0.3 is considered here for demonstration. (a) Step 1: Training data is selected from the middle, top, and bottom regions of the XRCT image. (b) Step 2: Selection of features, shown in Fig. 5. (c) Step 3: Train data using annotations. Red and blue annotations indicate features identified as aggregates and cement matrix. (d) Step 4: Get live feedback on training and retrain if needed. Aggregates and mortar are identified with distinct colors, with red and blue annotations identifying aggregates and cement matrix as in (c). (e) Step 5: Predict phase segmentation in XRCT images of concrete. (f) Step 6: Apply morphological operations and assign phases. Note: Air voids and high-density phase are obtained from intensity segmentation. (For interpretation of the references to color in this figure legend, the reader is referred to the web version of this article.)

2.5. Mesoscale simulations

The mesoscale simulations are used in the present work to demonstrate the implications of the phase segmentation accuracy on macroscale and microscale response. We considered two microstructures for mesoscale simulations — one with an accurate phase segmentation and the other with a less accurate or "perturbed" phase segmentation. The accuracy is determined based on the similarity between the size and shape of the segmented aggregates with those obtained from analysis of the aggregates in a dry shape, which is considered the ground truth. The subtleties in the two microstructures are discussed in detail in Section 3. XRCT images were transformed into a uniform hexahedral mesh to perform finite element simulations in the commercial software Abaqus. Each voxel was replaced by an equivalent hexahedral finite element. Only a cubical sub-region of each concrete sample with a side equal to 0.5 mm was modeled. This size was sufficiently large to examine the influence of phase segmentation on mesoscale simulations because there are no coarse aggregates in our concrete microstructures and our goal was to examine phase segmentation accuracy for two microstructures with the same size. A total of 1 million hexahedral finite elements were used to discretize the concrete microstructure. Two phases were considered for mesoscale simulations: aggregate phase and matrix phase. The aggregates were considered to be linear elastic with no material damage. The cement matrix was modeled as an elastic-plastic response with material damage. The widely used concrete damage plasticity (CDP) model was used for the

cement matrix. The CDP model accounts for compressive crushing and tensile cracking. A detailed description of the CDP model is provided in several Refs. [21,36] and is avoided here for brevity. The material parameters for the model were taken from [37] and are also provided to readers with Abaqus input files in the supplementary materials. The displacement-controlled loading is applied in 20 steps to produce an axial strain of 0.24% in the x and z directions. No displacement constraint is provided in the third direction (y-direction), resulting in a triaxial stress condition.

3. Results and discussion

3.1. Validation of phase segmentation

The visualization of phase segmentation results for the two approaches is presented in Fig. 7 for samples with aggregate volume fractions equal to 0.5, 0.4, 0.3, and 0.2. Fig. 7 shows the horizontal slices of raw data, corresponding segmented slices obtained from standard deviation thresholding and random forest segmentation, and the difference in binarized images (aggregates as 1 and cement matrix as 0) obtained from the two segmentation approaches. Visual examination suggests that both segmentation approaches perform satisfactorily in separating aggregates from the cement matrix for all aggregate volume fractions considered in this study. The concrete sample corresponding to an aggregate volume fraction equal to 0.2 had a large crack, as observed in Fig. 7(d). It is interesting to observe that the presence of

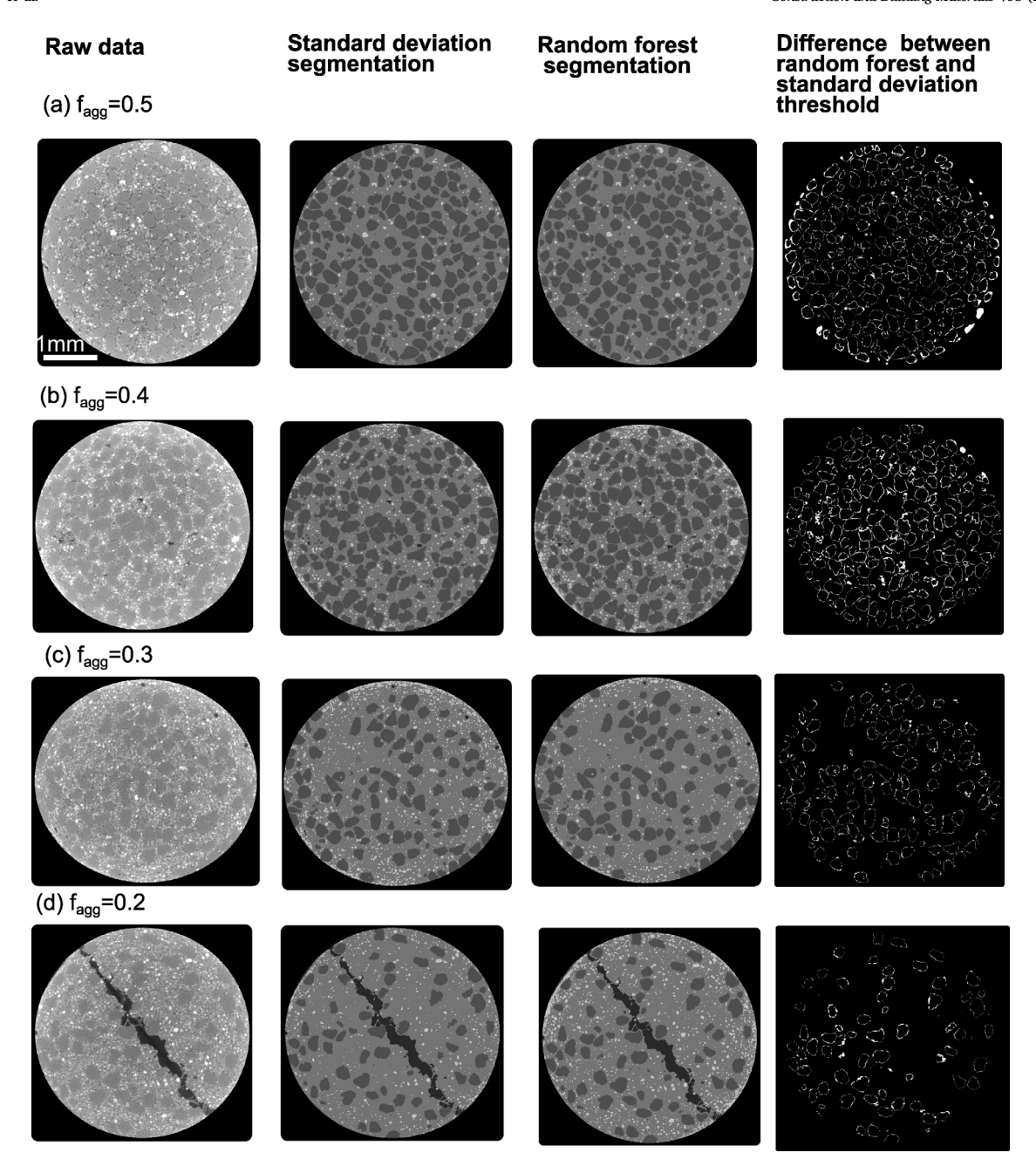


Fig. 7. Visualization of the phase segmentation results using deviation approach and random forest approach for different aggregate volume fractions. Aggregate volume fraction equal to (a) 0.5. (b) 0.4. (c) 0.3. (d) 0.1.

a crack did not influence the quality of phase segmentation using both approaches. The crack in the concrete sample with an aggregate volume fraction equal to 0.2 suggests that both phase segmentation approaches can also be used to segment cracked concrete samples, which is often of interest when XRCT imaging is performed *in-situ* e.g., [7]. We recall here that the segmentation of high-density phases and air voids from the cement matrix is straightforward; therefore, this segmentation is not discussed further. While segmented horizontal slices obtained from the random forest approach and standard deviation threshold indicate similar phase segmentation as shown in Fig. 7, the horizontal slices showing the difference between the two approaches reveal differences, particularly in capturing the edges of the grains. This led us to further examine how the two approaches differ in their ability to quantify both size and shape of grains.

Fig. 8 shows the distribution of aggregate size and aggregate shape parameters including sphericity, elongation index, and flatness index

for a concrete sample with aggregate volume fraction equal to 0.5 using both phase segmentation approaches. The same metrics are also shown for aggregates imaged in a dry condition prior to concrete sample preparation which is assumed as ground truth. Both approaches quantify the size and shape of the aggregates and are in close agreement with the ground truth. The validation of phase segmentation results for the concrete sample with an aggregate volume fraction equal to 0.3 is shown in Fig. 9 and is also in close agreement with the ground truth. The size of the aggregates, however, is not as accurate for a concrete sample with an aggregate volume fraction equal to 0.3 compared to a concrete sample with an aggregate volume fraction equal to 0.5. This difference in accuracy is not necessarily due to the differences in aggregate volume fraction, but rather related to fine adjustments in morphological operations used to obtain the final aggregate size and shape. Our goal while using morphological operations was to retrieve the volume of the aggregates closely while maintaining reasonable

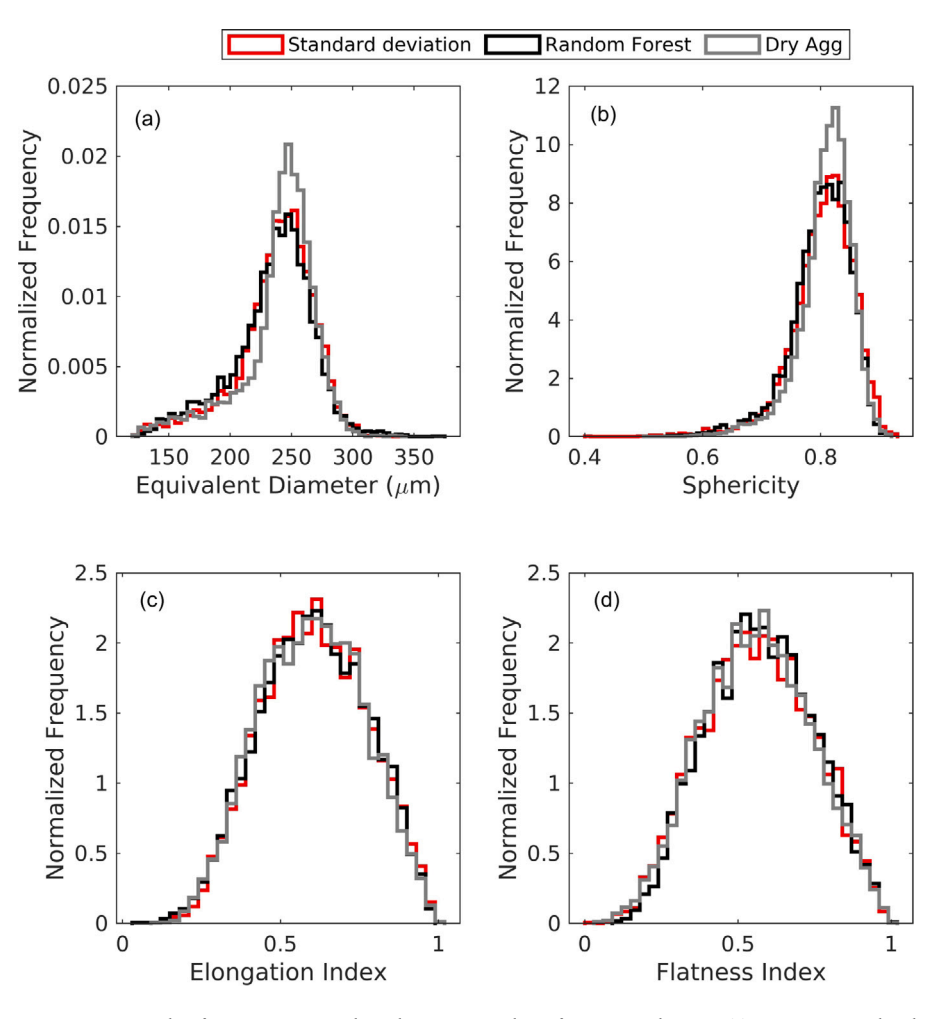


Fig. 8. Validation of image segmentation approaches for a concrete sample with aggregate volume fraction equal to 0.5. (a) Aggregate size distribution. (b) Aggregate sphericity distribution. (c) Aggregate elongation index distribution. (d) Aggregate flatness index distribution.

shapes. We further present the validation results for concrete samples with aggregate volume fractions equal to 0.4 and 0.2 in Figs. A.2 and A.3, respectively, in the Appendix A for brevity. It can be observed from Figs. A.2 and A.3 that the validation metrics, quantifying the shape and size of the aggregates, are in close agreement. This suggests the satisfactory performance of both phase segmentation approaches for all aggregate volume fractions considered in this study.

We further summarize phase segmentation results by quantifying aggregate volume fraction, mean sphericity, mean elongation index, and mean flatness index in Tables 1, 2, 3, and 4, respectively, for different aggregate volume fractions. The aggregate volume fraction in Table 1 is not quantified for the sample with the target aggregate volume fraction equal to 0.2 due to the presence of a large crack. The maximum change in volume fraction compared to the target aggregate volume fraction was observed to be 0.044 and 0.040 for standard deviation segmentation and random forest segmentation, respectively. The maximum change in mean sphericity compared to the ground truth was observed to be 0.018 and 0.015 for standard deviation thresholding segmentation and random forest segmentation, respectively. The maximum change in the mean elongation index compared to the ground truth was observed to be 0.018 and 0.024 for the standard deviation thresholding segmentation and random forest segmentation, respectively. The maximum change in the mean flatness index compared to the ground truth was observed to be 0.029 and 0.039 for standard deviation thresholding segmentation and random forest segmentation, respectively. All these results are close to the ground truth and demonstrate the usefulness of both phase segmentation approaches in separating the aggregate phase from the cement matrix.

Table 1 Aggregate volume fraction (f_{agg}) and change in aggregate volume fraction $(\delta f_{agg} = |f_{agg}^{larget} - f_{agg}|)$ obtained from segmentation of XRCT images using standard deviation segmentation and random forest segmentation. f_{agg}^{larget} represents the ground truth obtained from the aggregate volume fraction set during sample preparation.

$\mathbf{f}_{agg}^{target}$	Standard deviation segmentation		Random forest segmentation	
	f_{agg}	δf_{agg}	$\overline{\mathbf{f}_{agg}}$	δf_{agg}
0.5	0.498	0.002	0.491	0.009
0.4	0.444	0.044	0.391	0.009
0.3	0.271	0.029	0.260	0.04

Table 2 Mean sphericity of aggregates (S_{qgg}^{mean}) and change in mean sphericity of aggregates $(\delta S_{qgg}^{mean} = |S_{DY}, gagg}^{mean} - S_{qgg}^{mean}|)$ obtained from segmentation of XRCT images of concrete semples using standard deviation segmentation and random forest segmentation. $S_{DY}, gagg}^{mean}$ represents the ground truth which is the mean sphericity obtained from segmentation of the XRCT image of the dry aggregates before sample preparation.

$\mathbf{f}_{agg}^{target}$	S _{Dry agg} mean	Standard deviation segmentation		Random forest segmentation	
		S _{agg} ^{mean}	δS_{agg}^{mean}	S _{agg} ^{mean}	δS_{agg}^{mean}
0.5	0.808	0.803	0.005	0.800	0.008
0.4	0.817	0.793	0.024	0.802	0.015
0.3	0.816	0.798	0.018	0.808	0.008
0.2	0.826	0.815	0.011	0.811	0.015

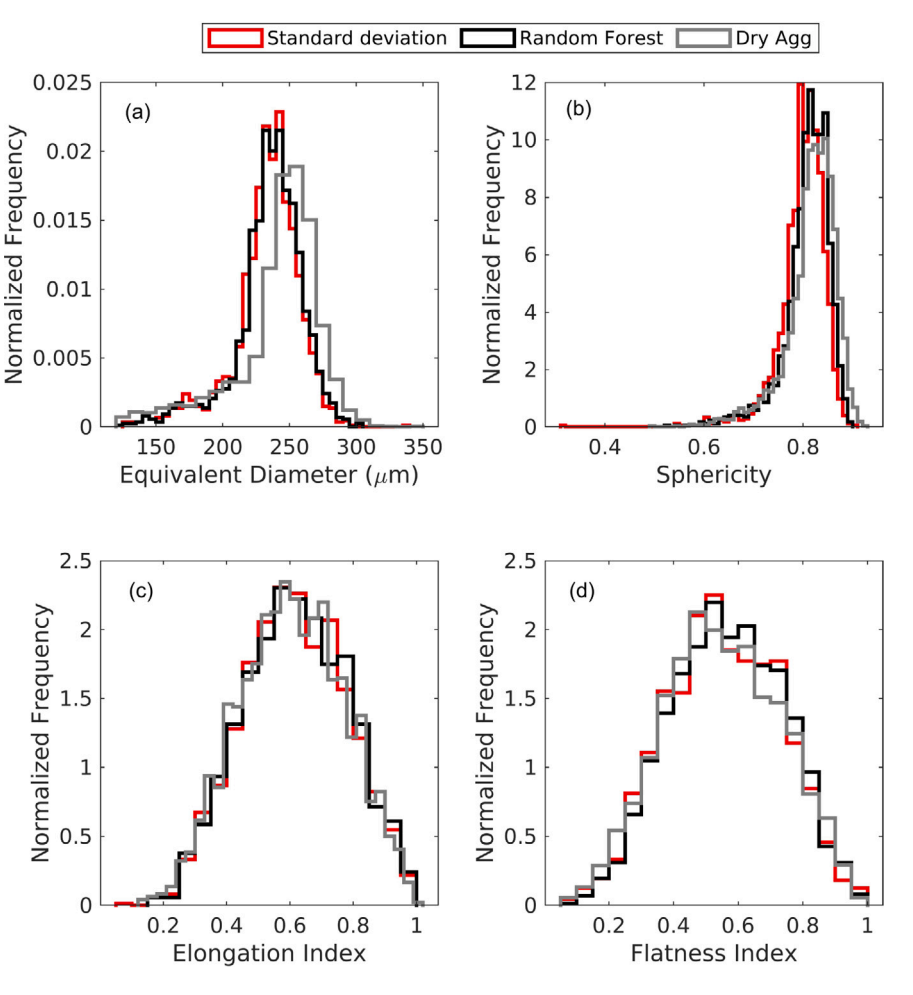


Fig. 9. Validation of image segmentation approaches for a concrete sample with aggregate volume fraction equal to 0.3. (a) Aggregate size distribution. (b) Aggregate sphericity distribution. (c) Aggregate elongation index distribution. (d) Aggregate flatness index distribution.

Table 3 Mean Elongation Index of aggregates (EI_{agg}^{mean}) and change in mean elongation index of aggregates ($\delta EI_{agg}^{mean} = EI_{Dr_{yagg}}^{mean} - EI_{agg}^{mean}$) obtained from segmentation of XRCT images of concrete samples using standard deviation segmentation and random forest segmentation. $EI_{Dr_{yagg}}^{mean}$ represents the ground truth which is the mean elongation index of aggregates obtained prior to sample preparation.

f ^{larget} agg	$\mathrm{EI}_{Dry}{}_{agg}^{mean}$	Standard deviation segm	lard deviation segmentation		gmentation
		EI _{agg}	δEI_{agg}^{mean}	EU _{agg}	δEI_{agg}^{mean}
0.5	0.599	0.607	0.008	0.603	0.004
0.4	0.603	0.605	0.002	0.608	0.005
0.3	0.605	0.614	0.009	0.617	0.012
0.2	0.596	0.614	0.018	0.620	0.024

Table 4 Mean Flatness index of aggregates (FI_{agg}^{mean}), change in mean flatness index of aggregates ($\delta FI_{agg}^{mean} = |FI_{Dr_j}|_{agg}^{mean} = FI_{Dr_j}|_{agg}^{mean}$) obtained from segmentation of XRCT images of concrete samples using standard deviation segmentation and random forest segmentation. $FII_{Dr_{agg}}^{mean}$ represents ground truth which is the mean flatness index of aggregates obtained prior to sample preparation.

$\mathbf{f}_{agg}^{target}$	$\mathrm{FI}_{Dry_{agg}}^{mean}$	Standard deviation segmentation		Random forest segmentation	
		FI _{agg} ^{mean}	δFI_{agg}^{mean}	FI _{agg} ^{mean}	δFI_{agg}^{mean}
0.5	0.560	0.563	0.003	0.573	0.013
0.4	0.552	0.581	0.029	0.591	0.039
0.3	0.549	0.553	0.003	0.566	0.017
0.2	0.540	0.557	0.017	0.565	0.025

3.2. Morphological operations in phase segmentation

The post-processing of phase segmentation data using morphological operations such as close and dilation has the potential to introduce error, particularly in capturing the shape of aggregates. We test this claim by considering two microstructures of a concrete sample with a target aggregate volume fraction of 0.5:

- a microstructure with the aggregate phase segmented using the standard deviation segmentation, as presented in the previous subsection and referred to as the "actual" segmentation or microstructure:
- a microstructure with aggregate phase segmented using standard deviation segmentation, but subjected to cleaning with different sizes of structuring elements in morphological operations as compared to the actual segmentation and referred to as the "perturbed" segmentation or microstructure.

The two cases were only generated for the standard deviation segmentation approach because the results in the previous subsection established similar performances of the standard deviation segmentation and random forest segmentation. The actual segmentation was closed by 4 voxels and dilated by 1 voxel, whereas the perturbed segmentation was closed by 2 voxels with no dilation. The aggregate size and shape metrics for the microstructure with the actual and perturbed segmentations for a concrete sample with a target aggregate volume fraction equal to 0.5 are presented in Fig. 10.

Fig. 10, in our opinion, reveals a remarkable behavior of morphological operations. Small changes in such operations can result in

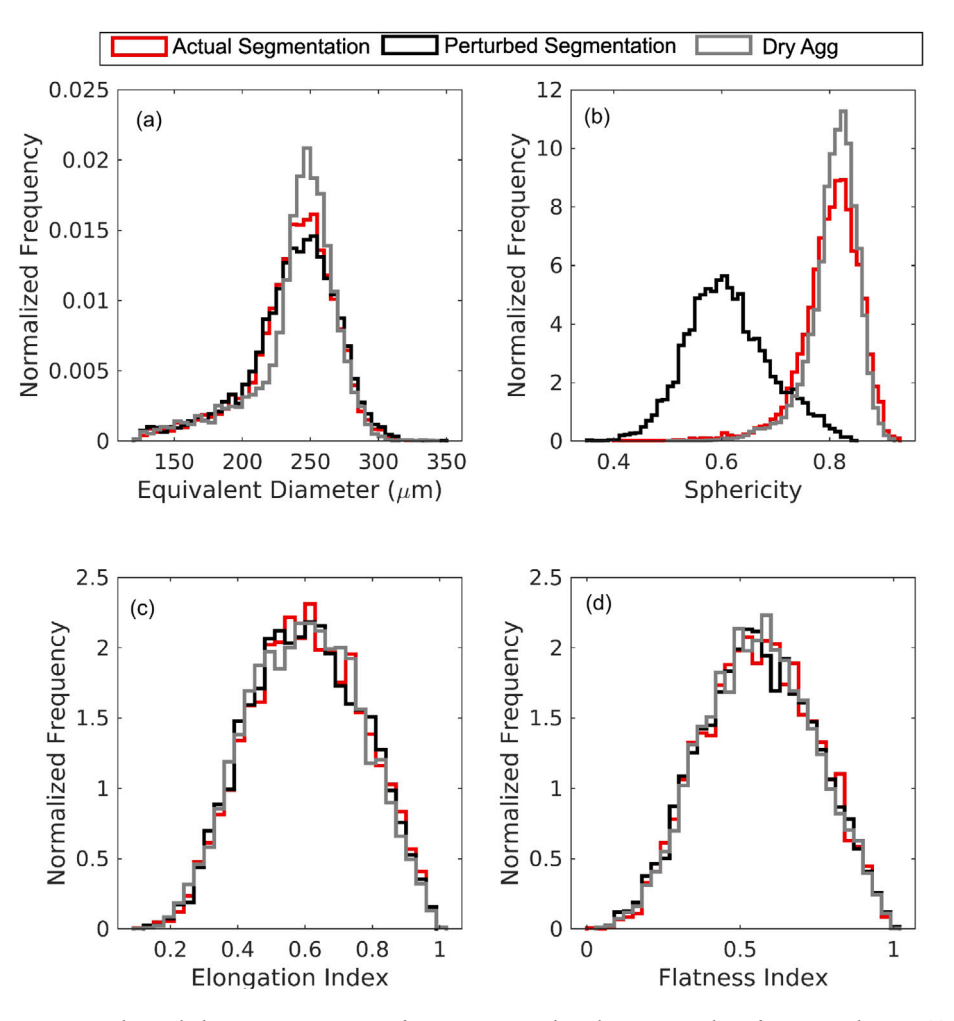


Fig. 10. Actual aggregate segmentation and perturbed aggregate segmentation for a concrete sample with aggregate volume fraction equal to 0.5. (a) Aggregate size distribution. (b) Aggregate sphericity distribution. (c) Aggregate elongation index distribution. (d) Aggregate flatness index distribution.

significant changes to aggregate sphericity while other size and shape metrics remain the same. A prior study by Stamati et al. [17] considered only aggregate size distribution for validating the accuracy of the phase segmentation approach. According to Fig. 10, if only aggregate size distribution was used to validate the phase segmentation results, both the microstructures would be considered satisfactory. Fig. 10(b), however, clearly suggests an error in the "perturbed" microstructure – the sphericity of the aggregates is seen to significantly deviate from the actual sphericity. Does this difference in the sphericity of aggregates in the two microstructures lead to a significant difference in macroscale and microscale response? We address this question by conducting mesoscale simulations on the actual segmentation microstructure and the perturbed segmentation microstructure, as discussed in the next subsection.

3.3. Implications of phase segmentation in mesoscale modeling

We used example microstructures discussed in the previous subsection – the actual segmentation microstructure and the perturbed segmentation microstructure – to conduct mesoscale simulations for a concrete sample with target aggregate volume fractions equal to 0.5. The microstructures were subjected to displacement-controlled loading to produce a triaxial stress state as described in Section 2. Fig. 11 shows the macroscopic axial stress–strain curves in one of the loading directions and the evolution of damage energy with the increase in axial strain. The peak stress, the strain corresponding to peak stress, and the damage energy were significantly different for actual microstructure

and perturbed microstructure. The peak stress increased by 16.24% and damage energy increased by 62.68% in the perturbed microstructure compared to the actual microstructure for a concrete sample with a target aggregate volume fraction equal to 0.5. There was no significant change in the modulus/stiffness of the two microstructures, which is expected because only the sphericity of aggregates changed and stiffness primarily depends on aggregate volume fraction. We further examined the damage initiation and damage propagation in Fig. 12 for the two cases by visualizing the damage in finite element simulations at various axial strains. We observe that the phase segmentation influences damage initiation significantly, as shown in Fig. 12(a) and (a') and Fig. 12(b) and (b'). The final damage pattern exhibits significant similarities with some minor differences, as observed in Fig. 12(c) and (c').

3.4. Perspective

It is clear that phase segmentation quality in XRCT images of concrete needs to be verified based on metrics that capture both aggregate size and aggregate shape. The use of XRCT imaging and mesoscale simulations in concrete is expected to increase, especially with the wider availability of imaging facilities and improvements in computing power. Therefore, it is critical for investigators to minimize the errors in building these mesoscale models. Phase segmentation is one of the steps towards building mesoscale models directly from XRCT-imaged microstructures. Other steps, such as image acquisition and calibration of mesoscale models may introduce additional errors. It is understandable

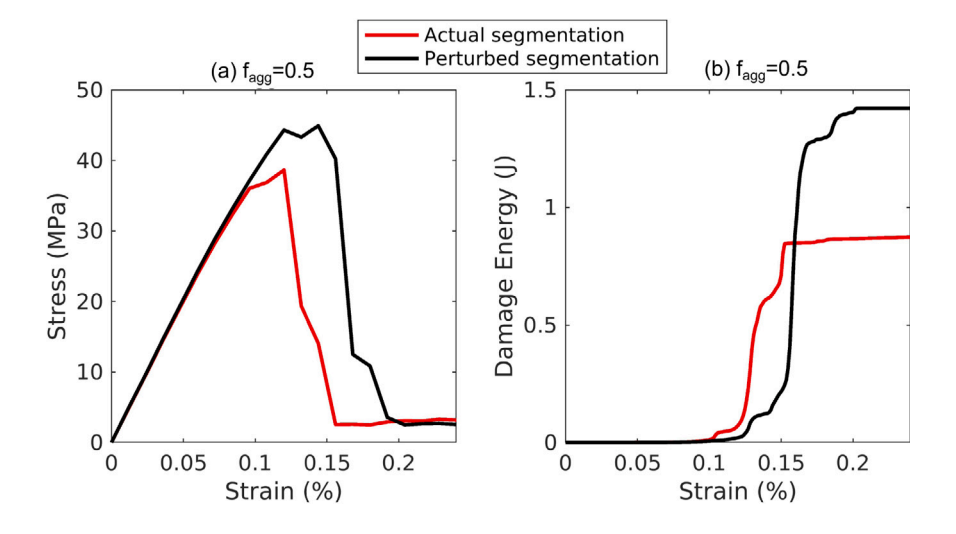


Fig. 11. Macroscopic response of concrete samples with actual segmentation and perturbed segmentation when subjected to triaxial loading conditions in mesoscale simulations. (a) Average axial stress–strain response in one of the loading directions (z-direction) for a concrete sample with aggregate volume fraction equal to 0.5. (b) Damage energy for a concrete sample with aggregate volume fraction equal to 0.5.

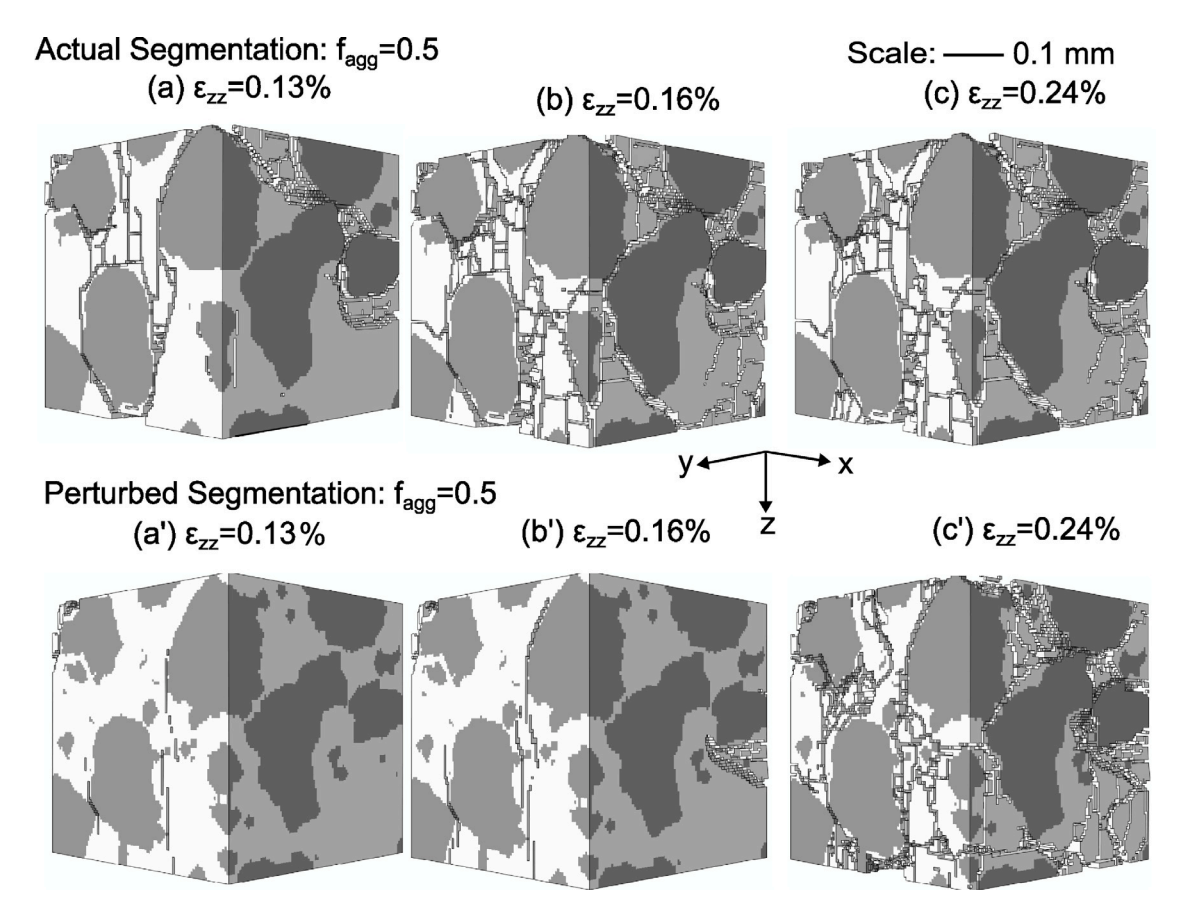


Fig. 12. Visualization of damage in mesoscale models of concrete with aggregate volume fraction equal to 0.5 for the actual microstructure ((a), (b), and (c)), and the perturbed microstructure ((a'), (b'), and (c')). Note the mesoscale models are $0.5 \times 0.5 \times 0.5 \times 0.5$ mm sub-volumes of XRCT scans of a larger sample as described in the main text.

that the validation of the phase segmentation may require additional resources and effort. For instance, in this study, XRCT images of dry aggregates were captured to serve as ground truth. Stamati et al. [17] used neutron imaging to validate phase segmentation results. We, therefore, suggest a few simple steps to verify the accuracy of phase segmentation images of concrete:

- Note the aggregate volume fraction of the concrete sample and use it to validate aggregate volume fraction in XRCT images of concrete.
- 2. Measure the dry aggregate size distributions using sieve analysis or XRCT imaging of the dry aggregates to validate the size obtained from segmented XRCT images of concrete samples.

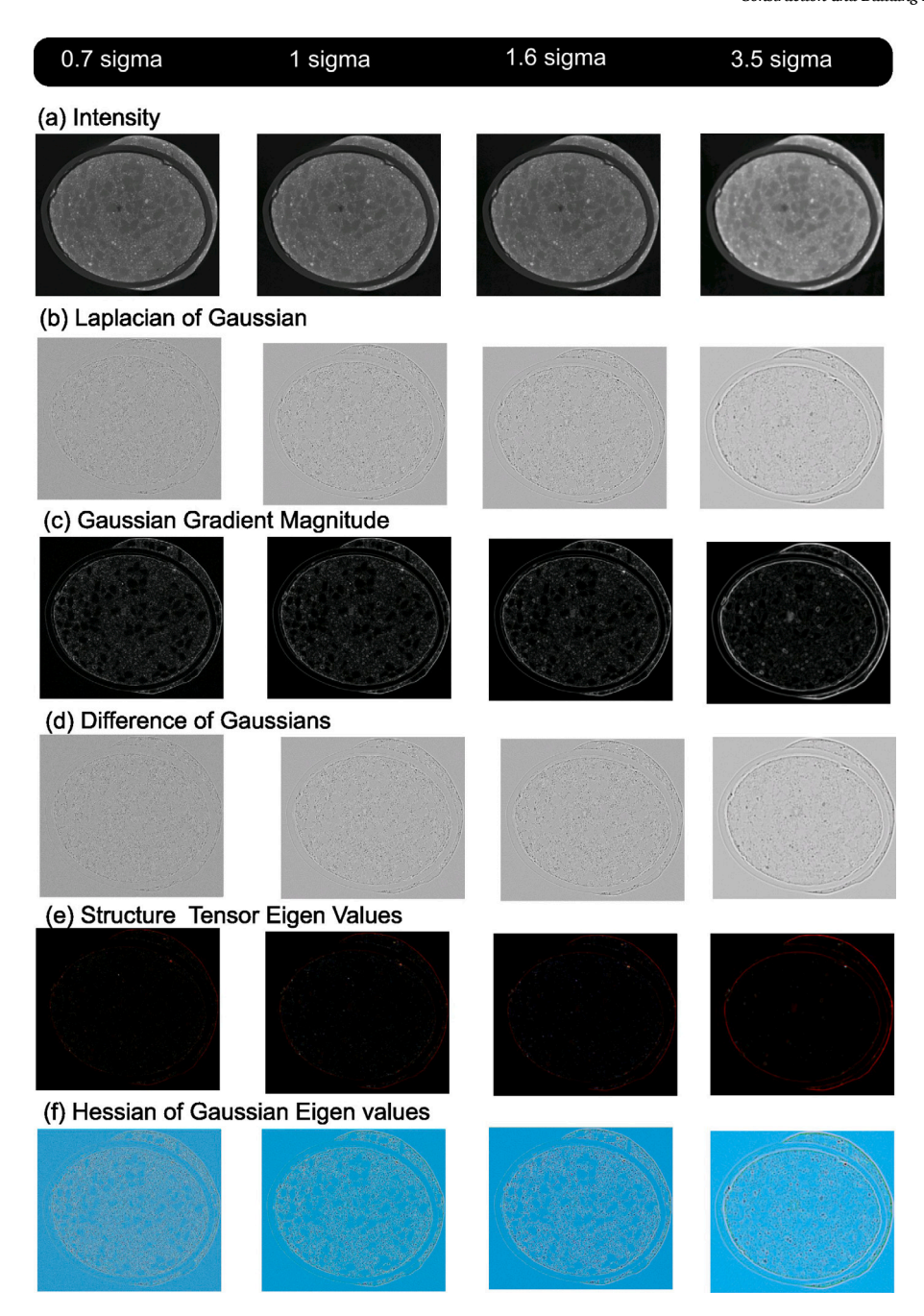


Fig. A.1. Visualization of the features that serve as input to random forest classification in ilastik. An aggregate volume fraction equal to 0.3 is considered here for demonstration. Features are chosen for the smoothing levels of 0.7 sigma (standard deviation), 1 sigma, 1.6 sigma, and 3.5 sigma. Therefore, a total of 25 features are considered including an additional intensity feature with sigma equal to 0.3 (not shown here). (a) Gaussian smoothing of raw data. (b) Laplacian of Gaussian. (c) Gaussian gradient magnitude. (d) Difference of Gaussian. (e) Structure tensor eigenvalues. (f) Hessian of Gaussian eigenvalues.

 Obtain aggregate shape-related metrics, preferably sphericity, from the literature to compare with the values obtained from the segmented images. Most of the aggregates that are used to prepare concrete have previously been characterized using XRCT imaging [35,38,39].

4. Conclusions

We examined the performance of two approaches – standard deviation thresholding and random forest classification – to segment aggregates in XRCT images of concrete with different aggregate volume fractions. The segmentation of the aggregate phase from the cement matrix is challenging due to their similar X-ray attenuation characteristics. Our results lead to important conclusions, as summarized below,

which can be beneficial for planning imaging studies and mesoscale modeling studies in the future:

1. We successfully validated the ability of both the segmentation approaches to segment the aggregate phase in concrete samples with aggregate volume fractions equal to 0.2, 0.3, 0.4, and 0.5. The random forest classification approach, implemented in open-source code ilastik, requires no programming experience. The standard deviation approach was implemented in an in-house MATLAB code provided to the reader in the Supplementary Materials. The standard deviation approach is fully automated and features minimal user input and thus features less user bias compared to the random forest approach which requires training via user annotations.

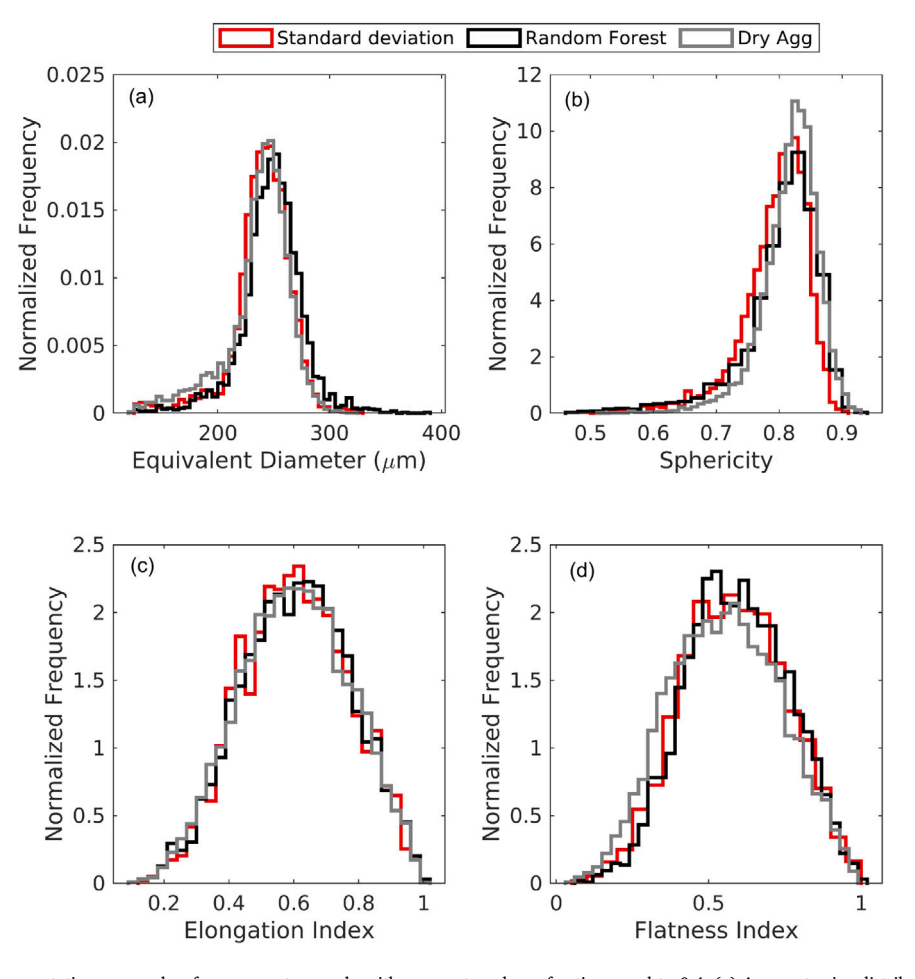


Fig. A.2. Validation of image segmentation approaches for a concrete sample with aggregate volume fraction equal to 0.4. (a) Aggregate size distribution. (b) Aggregate sphericity distribution. (c) Aggregate elongation index distribution. (d) Aggregate flatness index distribution.

- 2. The morphological operations required for post-processing segmented XRCT data have a tendency to deteriorate the shape of the aggregates if used without appropriate care. We therefore recommend verifying both aggregate size and aggregate shape metrics as described in Section 3.
- 3. Inaccurate aggregate shapes obtained through segmentation, even when aggregate size distributions are accurate, can significantly influence the accuracy of mesoscale simulations. We observed that a microstructure with an aggregate phase segmentation perturbed from a ground truth segmentation only by aggregate shape, while aggregate size distributions remained accurate, resulted in a 16.24% change in peak stress, and 62.68% change in damage energy.

CRediT authorship contribution statement

Mohmad M. Thakur: Writing – review & editing, Writing – original draft, Visualization, Validation, Formal analysis, Data curation, Conceptualization. Sean Enright: Visualization, Data curation. Ryan C. Hurley: Writing – review & editing, Supervision, Resources, Project administration, Funding acquisition, Conceptualization.

Declaration of competing interest

The authors declare the following financial interests/personal relationships which may be considered as potential competing interests: Ryan Hurley reports financial support was provided by National Science Foundation.

Data availability

Data will be made available on request.

Acknowledgments

All authors acknowledge support by the U.S. National Science Foundation Award No. CMMI-2125023. RCH thanks Edward Andò for the helpful discussions.

Appendix A

The features used as input to the random forest classifier in ilastik are summarized in Fig. A.1. A total of 25 features were selected to train the data and predict phase segmentation in X-ray images of concrete. 24 features are shown in Fig. A.1, and one additional feature, which represents raw data, is not shown in Fig. A.1 for brevity.

The validation of the phase segmentation approaches for concrete samples with aggregate volume fractions equal to 0.4 and 0.2 is presented in Figs. A.2 and A.3, respectively. Figs. A.2 and A.3 along with Figs. 8 and 9 demonstrate the effectiveness of the standard deviation thresholding approach and random forest segmentation approach in segmenting aggregates in concrete samples with different aggregate volume fractions. Both aggregate size and aggregate shape are captured precisely in both segmentation approaches.

Appendix B. Supplementary data

Supplementary material related to this article can be found online at https://doi.org/10.1016/j.conbuildmat.2023.133033.

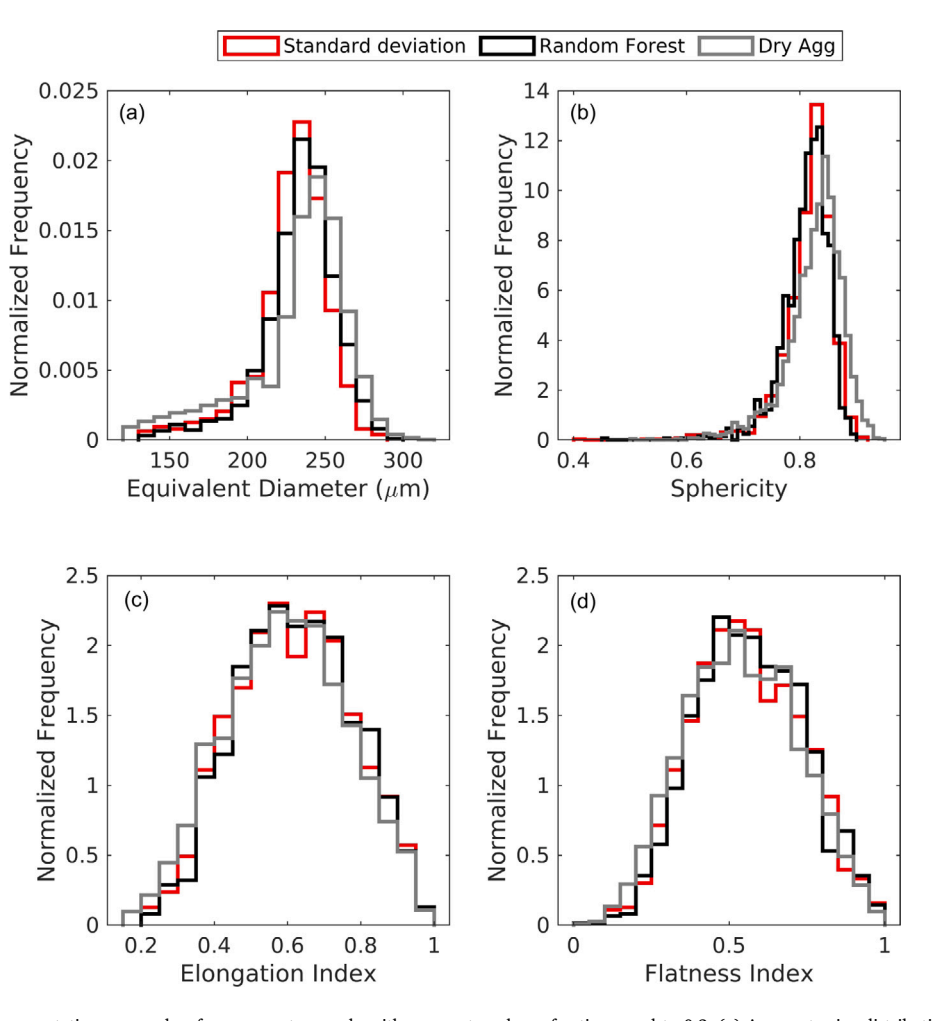


Fig. A.3. Validation of image segmentation approaches for a concrete sample with aggregate volume fraction equal to 0.2. (a) Aggregate size distribution. (b) Aggregate sphericity distribution. (c) Aggregate elongation index distribution. (d) Aggregate flatness index distribution.

References

- P.J. Monteiro, G. Geng, D. Marchon, J. Li, P. Alapati, K.E. Kurtis, M.J.A. Qomi, Advances in characterizing and understanding the microstructure of cementitious materials, Cem. Concr. Res. 124 (February) (2019) http://dx.doi.org/10.1016/j. cemconres.2019.105806.
- [2] S. Diamond, The microstructure of cement paste and concrete A visual primer, Cem. Concr. Compos. 26 (8) (2004) 919–933, http://dx.doi.org/10.1016/ j.cemconcomp.2004.02.028.
- [3] Z. Yang, W. Ren, R. Sharma, S. McDonald, M. Mostafavi, Y. Vertyagina, T.J. Marrow, In-situ X-ray computed tomography characterisation of 3D fracture evolution and image-based numerical homogenisation of concrete, Cem. Concr. Compos. 75 (2017) 74–83, http://dx.doi.org/10.1016/j.cemconcomp.2016.10.
- [4] P. Wriggers, S.O. Moftah, Mesoscale models for concrete: Homogenisation and damage behaviour, Finite Elem. Anal. Des. 42 (7 SPEC. ISS.) (2006) 623–636, http://dx.doi.org/10.1016/j.finel.2005.11.008.
- [5] S.-M. Kim, R.K.A. Al-Rub, Meso-scale computational modeling of the plastic-damage response of cementitious composites, Cem. Concr. Res. 41 (3) (2011) 339–358.
- [6] D. Wei, R.C. Hurley, L.H. Poh, D. Dias-da Costa, Y. Gan, The role of particle morphology on concrete fracture behaviour: A meso-scale modelling approach, Cem. Concr. Res. 134 (2020) 106096.
- [7] R. Hurley, D. Pagan, An in-situ study of stress evolution and fracture growth during compression of concrete, Int. J. Solids Struct. 168 (2019) 26–40.
- [8] S. Brisard, M. Serdar, P.J. Monteiro, Multiscale X-ray tomography of cementitious materials: A review, Cem. Concr. Res. 128 (2020) 105824.
- [9] R.C. Hurley, D.C. Pagan, E.B. Herbold, C. Zhai, Examining the micromechanics of cementitious composites using in-situ X-ray measurements, Int. J. Solids Struct. (2023) 112162.
- [10] A. Tsitova, F. Bernachy-Barbe, B. Bary, S.A. Dandachli, C. Bourcier, B. Smaniotto, F. Hild, Damage quantification via digital volume correlation with heterogeneous mechanical regularization: Application to an in situ meso-flexural test on mortar,

- [11] M.M. Thakur, N.A. Henningsson, J. Engqvist, P.-O. Autran, J.P. Wright, R.C. Hurley, On mesoscale modeling of concrete: Role of heterogeneities on local stresses, strains, and representative volume element, Cem. Concr. Res. 163 (2023) 107031
- [12] W. Trawiński, J. Tejchman, J. Bobiński, A three-dimensional meso-scale modelling of concrete fracture, based on cohesive elements and X-ray μCT images, Eng. Fract. Mech. 189 (2018) 27–50, http://dx.doi.org/10.1016/j.engfracmech. 2017.10.003.
- [13] M.A. Homel, J. Iyer, S.J. Semnani, E.B. Herbold, Cement and concrete research mesoscale model and X-ray computed micro-tomographic imaging of damage progression in ultra-high-performance concrete, Cem. Concr. Res. 157 (October 2021) (2022) 106799, http://dx.doi.org/10.1016/j.cemconres.2022.106799.
- [14] N. Otsu, A threshold selection method from gray-level histograms, IEEE Trans. Syst. Man Cybern. 9 (1) (1979) 62–66.
- [15] L. Breiman, Random forests, Mach. Learn. 45 (2001) 5-32.
- [16] A. Tsitova, F. Bernachy-Barbe, B. Bary, C. Bourcier, F. Hild, Identification of microscale fracture models for mortar with in-situ tests, Int. J. Mech. Sci. 242 (2023) 107988.
- [17] O. Stamati, E. Roubin, E. Andò, Y. Malecot, Phase segmentation of concrete x-ray tomographic images at meso-scale: Validation with neutron tomography, Cem. Concr. Compos. 88 (2018) 8–16, http://dx.doi.org/10.1016/j.cemconcomp.2017. 12.011.
- [18] C. Sommer, C. Straehle, U. Koethe, F.A. Hamprecht, Ilastik: Interactive learning and segmentation toolkit, in: 2011 IEEE International Symposium on Biomedical Imaging: From Nano to Macro, IEEE, 2011, pp. 230–233.
- [19] S. Berg, D. Kutra, T. Kroeger, C.N. Straehle, B.X. Kausler, C. Haubold, M. Schiegg, J. Ales, T. Beier, M. Rudy, et al., Ilastik: interactive machine learning for (bio) image analysis, Nat. methods 16 (12) (2019) 1226–1232.
- [20] J. Kleesiek, A. Biller, G. Urban, U. Kothe, M. Bendszus, F. Hamprecht, Ilastik for multi-modal brain tumor segmentation, in: Proceedings MICCAI BraTS (Brain Tumor Segmentation Challenge), Vol. 12, Citeseer, 2014, p. 17.

- [21] S. Naderi, W. Tu, M. Zhang, Meso-scale modelling of compressive fracture in concrete with irregularly shaped aggregates, Cem. concr. res. 140 (2021) 106317.
- [22] M. Nitka, J. Tejchman, A three-dimensional meso-scale approach to concrete fracture based on combined DEM with X-ray μCT images, Cem. Concr. Res. 107 (2018) 11–29
- [23] S. Häfner, S. Eckardt, T. Luther, C. Könke, Mesoscale modeling of concrete: Geometry and numerics, Comput. struct. 84 (7) (2006) 450-461.
- [24] K. Wan, Q. Xu, Local porosity distribution of cement paste characterized by X-ray micro-tomography, Sci. China Technol. Sci. 57 (2014) 953–961.
- [25] M. Leite, P. Monteiro, Microstructural analysis of recycled concrete using X-ray microtomography, Cem. Concr. Res. 81 (2016) 38–48.
- [26] M. Lanzón, V. Cnudde, T. De Kock, J. Dewanckele, X-ray microtomography (μ-CT) to evaluate microstructure of mortars containing low density additions, Cem. Concr. Compos. 34 (9) (2012) 993–1000.
- [27] I. Viejo, L.P. Esteves, M. Laspalas, J.M. Bielsa, Numerical modelling of porous cement-based materials by superabsorbent polymers, Cem. Concr. Res. 90 (2016) 184–193.
- [28] P.J. Monteiro, G. Geng, D. Marchon, J. Li, P. Alapati, K.E. Kurtis, M.J.A. Qomi, Advances in characterizing and understanding the microstructure of cementitious materials, Cem. Concr. Res. 124 (2019) 105806.
- [29] MathWorks, Stdfilt, 2021, MathWorks website, accessed on: March 28, 2023 URL https://www.mathworks.com/help/images/ref/stdfilt.html.
- [30] P. Soille, et al., Morphological Image Analysis: Principles and Applications, Vol. 2, Springer, 1999.

- [31] P. Geurts, A. Irrthum, L. Wehenkel, Supervised learning with decision tree-based methods in computational and systems biology, Mol. Biosyst. 5 (12) (2009) 1593–1605.
- [32] iLASTIK Developers, iLASTIK interactive learning and segmentation toolkit, 2021, https://www.ilastik.org, Accessed: March 27, 2023.
- [33] iLASTIK Developers, Pixel classification with iLASTIK, 2021, https://www.ilastik. org/documentation/pixelclassification/pixelclassification.html, Accessed: March 27, 2023.
- [34] MathWorks, Image segmentation with watershed algorithm, 2021, https://www.mathworks.com/help/images/image-segmentation-with-watershedalgorithm.html, Accessed on: March 28, 2023.
- [35] R. Rorato, M. Arroyo, E. Andò, A. Gens, Sphericity measures of sand grains, Eng. geol. 254 (2019) 43–53.
- [36] Y. Huang, Z. Yang, W. Ren, G. Liu, C. Zhang, 3D meso-scale fracture modelling and validation of concrete based on in-situ X-ray computed tomography images using damage plasticity model, Int. J. Solids Struct. 67 (2015) 340–352.
- [37] A. Elkady, Github, 2023, https://github.com/amaelkady/abaqus-tools.
- [38] K.A. Alshibli, M.F. Jarrar, A.M. Druckrey, R.I. Al-Raoush, Influence of particle morphology on 3D kinematic behavior and strain localization of sheared sand, J. Geotech. Geoenviron. Eng. 143 (2) (2017) 04016097.
- [39] M.M. Thakur, D. Penumadu, Influence of friction and particle morphology on triaxial shearing of granular materials, J. Geotech. Geoenviron. Eng. 147 (11) (2021) 04021118.